Journal of Nuclear Materials 378 (2008) 305–311

Contents lists available at ScienceDirect

Journal of Nuclear Materials

journal homepage: www.elsevier.com/locate/jnucmat

Ductile–brittle transition of polycrystalline iron and iron–chromium alloys

Masaki Tanaka *,[1], Angus J. Wilkinson, Steve G. Roberts

Department of Materials, University of Oxford, Parks Road, Oxford, OX1 3PH, UK

ARTICLE INFO

PACS:
61.72.Lk

ABSTRACT

Fracture toughness of polycrystalline Fe, Fe–3%Cr and Fe–9%Cr was measured by four-point bending of pre-cracked specimens at temperatures between 77 K and 150 K and strain rates between 4.46×10^{-4} and 2.23×10^{-2} s^{-1}. For all materials, fracture behaviour changed with increasing temperature from brittle to ductile at a distinct brittle–ductile transition temperature (T_c), which increased with increasing strain rate. At low strain rates, an Arrhenius relation was found between T_c and strain rate in each material. At high strain rates, T_c was at slightly higher values than those expected from extrapolation of the Arrhenius relation from lower strain rates. This shift of T_c was associated with twinning near the crack tip. For each material, use of an Arrhenius relation for tests at strain rates at which specimens showed twinning gave the same activation energy as for the low strain rate tests. The values of activation energy for the brittle–ductile transition of polycrystalline Fe, Fe–3%Cr and Fe–9%Cr were found to be 0.21, 0.15 and 0.10 eV, respectively, indicating that the activation energy for dislocation glide decreases with increasing chromium concentration in iron.

1. Introduction

Fusion power has attracted great interest due to its potential as a major power source for the mid 21st century onwards. Reduced-activation ferritic–martensitic (RAFM) steels based on iron ~9% chromium form one of the classes of materials currently anticipated for structural components of the proposed DEMO reactor and future power plants [1,2]. In critical applications in the 'first wall', such materials will be exposed to high doses (several dpa/year) of 14 MeV neutrons, resulting in embrittlement and increased ductile–brittle transition temperature (DBTT) [3]. The brittle–ductile transition temperature (T_c) for a wide range of ferritic/martensitic steels varies over a ~100 °C range with Cr content and follows the same pattern of variation with Cr content in all steels studied, with a minimum in DBTT at 5–10% Cr [1,4]. The upward shift in T_c (ΔT_c) after irradiation (7–36 dpa at 365–410 °C) also follows a common pattern with Cr content across all steels studied, with a very small shift at 9% Cr [5], rising to a shift of 200–250 °C at low (2%) or high (12%) Cr contents; Cr content has a stronger influence on ΔT_c than other compositional or microstructural factors (at least under conditions with little He production). Post-irradiation swelling also varies strongly with Cr content [6]. There is thus a need to understand the influence of Cr on DBT behaviour in simple Fe–Cr binaries, to underpin understanding of DBT behaviour in more complex RAFM alloys such as Eurofer97 [7].

Many unirradiated body-centred cubic (BCC) metals show a gradual DBT where fracture toughness increases with increasing temperature up to T_c, over a range of 100 K or more [8–11], though some BCC metals such as single-crystal Fe–3%Si [12] have been found to exhibit a 'sharp' transition where fracture toughness is roughly constant below T_c, then increases over a few degrees at T_c. Such 'sharp transition' behaviour is also seen in semiconductors and ceramics such as Si and Al_2O_3, where it has been attributed to a near-zero initial dislocation density [13–15].

In many materials [16], including semiconductors [13,14,17,18], ceramics [15,19], intermetallics [20,21] and BCC metals [9,11,16,22], it has been found that the relation between T_c and strain rate, $\dot{\varepsilon}$, is empirically given by an Arrhenius equation as follows:

$$\dot{\varepsilon} = A \cdot \exp(-E_a/kT_c), \tag{1}$$

where A is a prefactor, E_a is the activation energy for the DBT and k is Boltzmann's constant. For a given material, the activation energy for the DBT is found to be close to the activation energy for dislocation glide, strongly suggesting that the DBT in these materials is controlled by dislocation glide. In BCC metals, screw dislocations move much more slowly than edge dislocations at the same resolved shear stress, so that generally the rate of emission of dislocations from crack tip sources is controlled by the motion of screw dislocation. In the experiments on single-crystal tungsten performed by Gumbsch et al. [9], they selected a uniquely special crystallographic orientation of specimen that allowed easy emission of

* Corresponding author. Tel./fax: +81 92 802 2952.
E-mail address: masaki@zaiko.kyushu-u.ac.jp (M. Tanaka).
[1] Present address: Department of Materials Science and Engineering, Kyushu University, 744 Motooka, Fukuoka 819-0395, Japan.

0022-3115/$ - see front matter © 2008 Elsevier B.V. All rights reserved.
doi:10.1016/j.jnucmat.2008.06.039

edge dislocation segments from the crack tip, giving a much lower activation energy than that found for tungsten of other orientations and in polycrystalline tungsten [11]; this reinforces the conclusion that generally in BCC metals, the motion of screw dislocations controls the DBT behaviour.

Models based on dislocation-dynamics simulation of plastic-zone evolution and their effects of crack tip stress fields ('shielding') have been successful in modelling the DBT in silicon crystals [23] and other materials [24]. For pure iron and simple binary alloys, the application of such models is not currently possible, because of the very limited data available for fracture toughness and the DBT (including strain rate effects) or dislocation mobility. The aim of the current study is to provide fracture and DBT data suitable for such modelling, which will be reported elsewhere.

In the present study, the effects of chromium content on the DBT of polycrystalline iron–chromium were experimentally studied, using chromium concentrations of 0%, 3% and 9%. For each alloy composition, fracture toughness was measured over a range of temperatures at several strain rates. Values of activation energy for the DBT in each alloy were derived from the variation of the DBT temperature, T_c, with strain rate, using Eq. (1).

2. Experimental procedures

Polycrystalline Fe, Fe–3%Cr and Fe–9%Cr with grain sizes in the range 90–300 μm were supplied by Metal Crystals and Oxides, Cambridge, UK. The chemical composition of the materials used are shown in Table 1. The Fe and Fe–Cr alloys have different C concentrations (0.0119, 0.0018 and 0.0021 mass% for Fe, Fe–3%Cr and Fe–9%Cr, respectively). Although impurity carbon atoms can pin both edge and screw dislocations, they are not likely to have a significant effect on dislocation motion once the dislocations are unpinned [25,26]. Since the dislocation sources, close to the crack tip, will be subjected to very high stresses, while the initial operation of the sources and the emission of their first dislocation might be slightly inhibited, the continued operation of the source will not. Since the DBT in metals is associated with substantial dislocation activity at the crack tip, we do not expect that the levels of carbon found in these materials will substantially affect their DBT behaviour.

Bend specimens $1 \times 1 \times 11$ mm^3 were cut using a Buehler 'isomet' saw. Each surface was then ground and polished, with the final polishing stage using 1μm diamond paste on a soft cloth. The sample size is relatively small, compared to, for example, ASTM standard bend specimens. However, it has been shown that while the absolute value of DBT temperature at a given strain rate depends on specimen size and geometry [11,24], the value of activation energy for DBT derived varying the strain rate in experiments using a fixed specimen size and geometry does not depend on the specimen type. Therefore, once a value of activation energy is obtained for a given specimen type and material and the DBT is determined at one strain rate, Eq. (1) can be used to predict DBT temperatures at other strain rates.

Notches with sharp cracks at their bases were produced on the tensile surface of each specimen by electro-discharge machining, using a razor blade as a sharp-edged tool to produce a notch ~80 μm deep. The radius at the notch tip was found to be ~30 μm.

Four-point bend tests were carried out at surface strain rates from 4.46×10^{-4} to 2.23×10^{-2} s^{-1}. The test temperature was controlled by using liquid nitrogen at 77 K and cold nitrogen gas from 100 K to 150 K. In each test, temperature variation was controlled to within ±0.5 K.

3. Results and discussion

3.1. Fe–9%Cr: Four-point bend tests

Fig. 1 shows typical stress–strain curves from Fe–9%Cr tested at a maximum strain rate of 4.46×10^{-4} s^{-1}, illustrating three characteristic deformation modes. Curve (a) (77 K) indicates brittle fracture, where fracture took place without any appreciable plastic deformation. Curve (b) (100 K) indicates semi-brittle fracture, where plastic deformation is seen slightly before fracture. Curve (c) (140 K) shows ductile bending, where the sample continued to deform plastically after yielding. In the test jig used, samples could not be deformed to more than ~3.5% total (elastic + plastic) strain, so the deformation mode was defined as 'ductile' if samples did not fracture up to this point.

Figs. 2(a) and (b) show fracture surfaces of the samples in Fig. 1(a) and (b), respectively. The cross section of the notch is seen at the top of the figures, and cracks propagated from the root of the notch. Fig. 2(a) (77 K) exhibits transgranular cleavage over the whole surface, indicating purely brittle fracture. In Fig. 2(b) (100 K), most of the surface shows cleavage; however, there are also regions of ductile tearing to depths of a few hundred microns below the notch root. Thus in semi-brittle fracture, it appears that some plastic deformation take place in a small region around the pre-crack but final fracture itself occurs in a brittle manner. This is in good agreement with curve (b) in Fig. 1, which exhibits slight plastic deformation before fracture occurs.

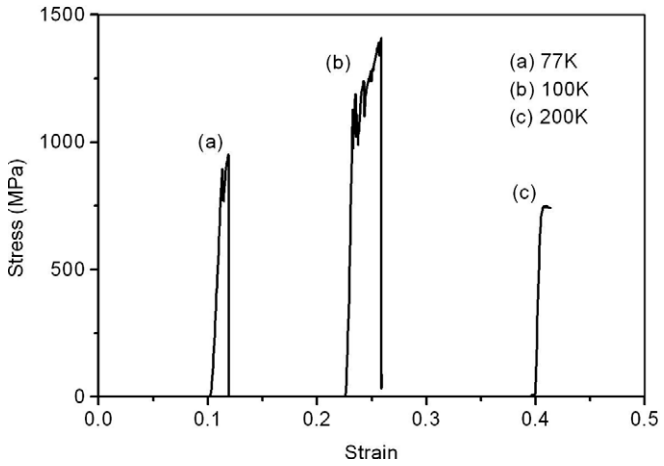

Fig. 1. Stress–strain curves from four-point bend tests of Fe–9%Cr at a strain rate of 4.46×10^{-4} s^{-1}. (a) 77 K: brittle fracture; (b) 100 K: semi-brittle fracture; (c) 200 K: ductile bending.

Table 1
Chemical compositions of the materials used

	C (mass %)	Si (mass %)	Mn (mass %)	P (mass %)	S (mass %)	Cr (mass %)
Fe	0.0119	<0.01	<0.01	<0.004	<0.001	<0.01
Fe–3%Cr	0.0018	0.01	0.39	<0.004	<0.001	3.11
Fe–9%Cr	0.0021	<0.01	<0.01	<0.004	<0.001	8.82

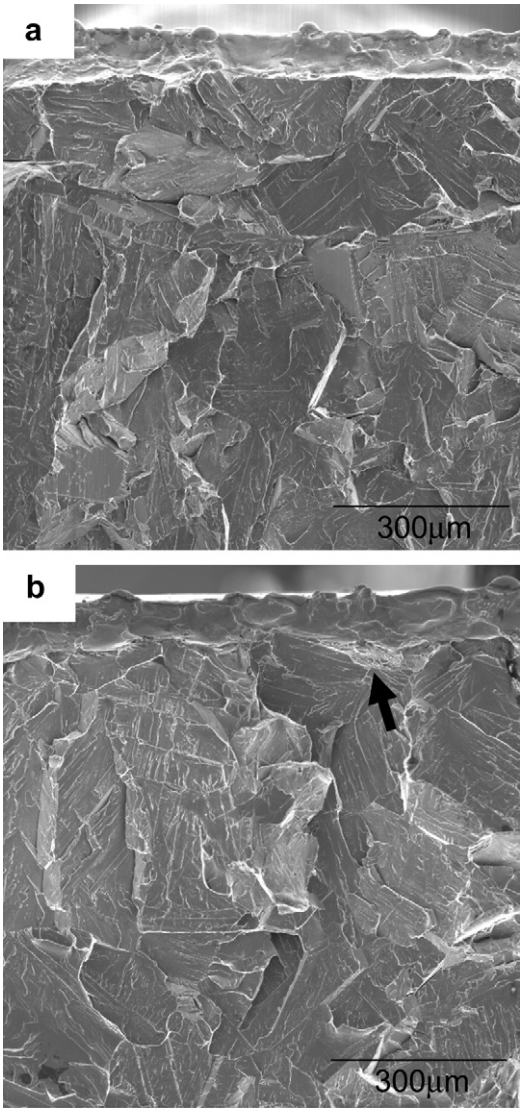

Fig. 2. SEM images of fracture surfaces of Fe–9%Cr. The strain rate used was $4.46 \times 10^{-4}\,s^{-1}$. (a) Specimen tested at 77 K, showing a typical brittle fracture surface, (b) specimen tested at 100 K, showing semi-brittle behaviour; ductile voids are seen in a small area indicated by an arrow in the figure.

Fracture toughness, K_{IC}, in a four-point bending test is given by

$$K_{IC} = \sigma_f \sqrt{\pi c} f(\xi), \quad \xi = c/h,$$
$$f(\xi) = 1.112 - 1.40\xi + 7.33\xi^2 - 13.08\xi^3 + 14.0\xi^4, \qquad (2)$$

where σ_f is the fracture stress, c is the crack length and h is the specimen height [27]. The fracture toughness was measured between 77 K and 130 K and at strain rates from $4.46 \times 10^{-4}\,s^{-1}$ to $2.23 \times 10^{-2}\,s^{-1}$. For ductile specimens, values of yield stress were used for σ_f in Eq. (2) instead of fracture stress, giving a lower-bound value for the fracture toughness.

Fig. 3(a)–(c) shows fracture toughness versus temperature for Fe–9%Cr at strain rates of 4.46×10^{-4}, 8.93×10^{-4} and $4.46 \times 10^{-3}\,s^{-1}$. Solid squares, triangles and circles represent brittle fracture, semi-brittle fracture and ductile bending, respectively. For ductile behaviour, since the specimens did not fracture, the 'fracture toughness' values shown are lower-bound values calculated from yield stress in each test and the notch/crack depths. The arrows above the solid circles mean that the real values of fracture toughness are higher than those indicated. The fracture toughness at 77 K seems to vary slightly with strain rate, however, there is some scatter due to the polycrystalline nature of the material,

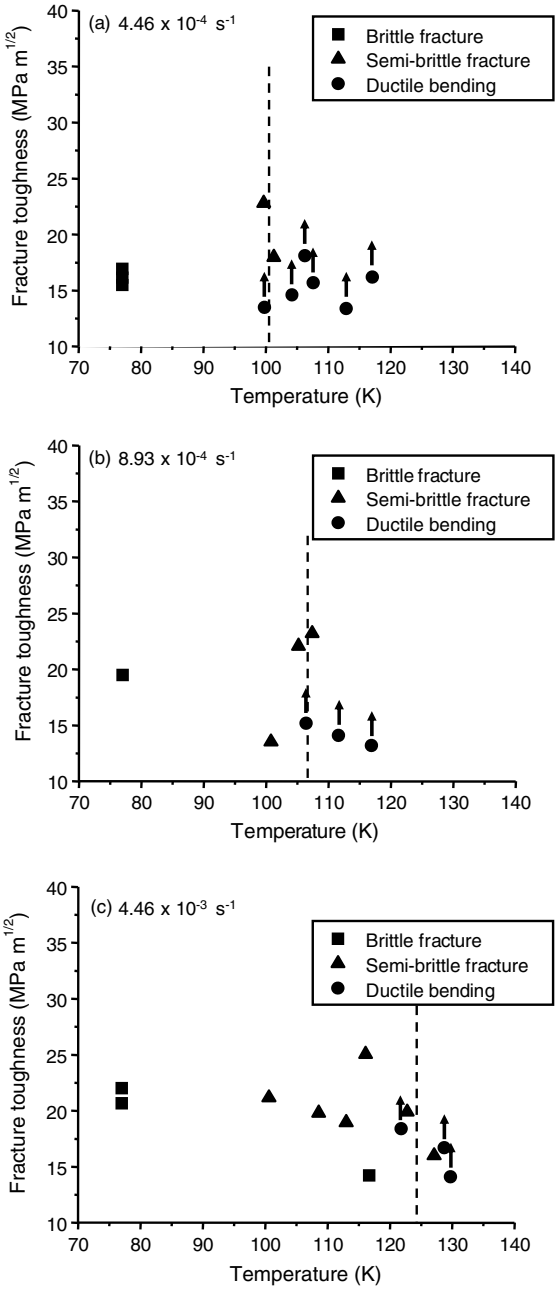

Fig. 3. Fracture toughness as a function of temperature for Fe–9%Cr, tested at strain rates of: (a) $4.46 \times 10^{-4}\,s^{-1}$, (b) $8.93 \times 10^{-4}\,s^{-1}$, (c) $4.46 \times 10^{-3}\,s^{-1}$. Solid squares, triangles and circles represent brittle fracture, semi-brittle fracture and ductile bending, respectively. Dashed lines indicate the brittle–ductile transition temperature. Increasing the strain rate increases the brittle–ductile transition temperature.

with only a few grains of different crystallographic orientation across the crack front in each sample, so no clear trend can be identified. The DBT temperature, T_c, indicated by dashed lines in Fig. 3, is taken as the mean of the highest temperature for semi-brittle fracture and the lowest temperature for ductile bending. Generally, fracture toughness close to the DBT is slightly higher than at 77 K. The determination of T_c is inevitably somewhat uncertain due to the large grain size (relative to specimen size), with each grain differently orientated with respect to the applied stresses near the notch. However, the uncertainties in the DBT at a given strain rate are rather smaller than the shifts in DBT with strain rate (see Fig. 4).

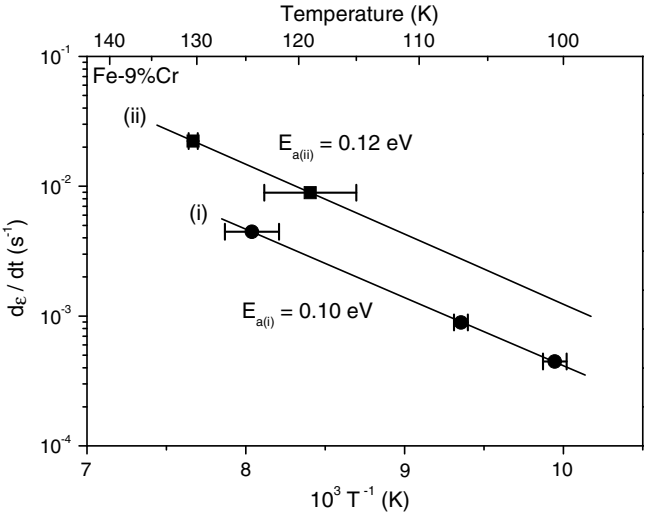

Fig. 4. Arrhenius plot of ln(strain rate) as a function of reciprocal transition temperature for polycrystalline Fe–9%Cr. Solid squares indicate strain rates where twinning was observed near the crack tip; solid circles indicate that no twinning was seen. Lines fitted to these two types of test results have the same slope, implying that the critical process in each case has the same activation energy. Error bars indicate the highest temperature for semi-brittle fracture and the lowest temperature for ductile bending.

Fig. 4 shows an Arrhenius plot of the ln(strain rate) vs $1/T_c$ for Fe–9%Cr tested at strain rates of 4.46×10^{-4}, 8.93×10^{-4}, 4.46×10^{-3}, 8.93×10^{-3} and $2.23 \times 10^{-2}\,s^{-1}$. The data do not fit on a single straight line. Instead, two parallel lines are drawn; the reasons for this are given below.

3.2. Fe–9%Cr: scanning electron microscopy (SEM)/electron backscattered diffraction (EBSD) observations around crack tips

Fig. 5(a) and (c) shows SEM images of crack tips of Fe–9%Cr samples deformed at strain rates of $4.46 \times 10^{-4}\,s^{-1}$ (the lowest strain rate used) and $8.93 \times 10^{-3}\,s^{-1}$ (the second-highest strain rate used), after electropolishing for subsequent EBSD observation. Fig. 5(e) shows a higher magnification view of the crack tip in Fig. 5(c). The specimens were deformed at 117 K, which in both cases is higher than T_c, i.e., both deformed by ductile bending, to strains of 3.0×10^{-2} (Fig. 5(a)) and 3.5×10^{-2} (Fig. 5(c)). The electron backscattered diffraction (EBSD) images in Fig. 5(b), (d) and (f) indicates the crystallographic orientations of grains around the crack tips shown in Figs. 5(a), (c) and (e). The colour indicates the orientation of the grains relative to the x direction in Fig. 5(h). A key to the colour mapping is given in Fig. 5(g).

Fig. 5(b) shows that the crack in the specimen deformed at the lower strain rate stopped at a grain boundary. Rotations due to slip deformation can be seen ahead of the crack and in the grain immediately below the crack tip. Deformation was solely by slip at this temperature and strain rate (the lowest strain rate used).

For the specimen deformed at the higher strain rate, Fig. 5(d) shows crystallographically distinct areas (red) with widths of several microns around the crack tip. Fig. 5(e) shows an enlarged SEM image of the region close to the crack tip, and Fig. 5(f) shows an EBSD image of the area surrounded by a dashed rectangle in (e), indicating similar crystallographically distinct regions around the crack tip as blue lines. The grain boundaries between the red or blue regions and the matrix were found to be all of $\Sigma 3$ type, indicating that they are twins.

Thus even though the specimens shown in (a) and (c) were both deformed at the same temperature and in the ductile regime, their deformation processes were different. At low strain rates, only slip was observed, while for higher strain rates ($>8.93 \times 10^{-3}\,s^{-1}$), twins also developed at the crack tip. This difference in crack tip deformation mechanism, resulting in a lower T_c at high strain rates than would be expected from extrapolation of low strain rate behaviour, is why two lines are drawn on the Arrhenius plot in Fig. 4. One line, labelled (i) is fitted to the points for low strain rates of 4.46×10^{-4}, 8.93×10^{-4} and $4.46 \times 10^{-3}\,s^{-1}$, and the other, labelled (ii), is fitted to the points for high strain rates of 8.93×10^{-3} and $2.23 \times 10^{-2}\,s^{-1}$. The slope of line (i) gives a value of activation energy of 0.10 ± 0.001 eV while that of line (ii) gives 0.11 eV although given the possible errors of T_c measurements (due to the large grain size), these can only be tentative values. The value of the activation energy for the DBT thus appears not to be affected by the onset of twinning at higher strain rate, though the value of T_c shifts to lower temperatures. This implies that the glide of dislocations controls the DBT at all strain rates; at the higher strain rates, it is possible that intersection of glide planes with twins inhibits their dislocation motion, thus decreasing ductility.

3.3. Fe and Fe–3%Cr

Figs. 6(a) and (b) show Arrhenius plots of the strain rate and transition temperature for polycrystalline Fe–3%Cr and polycrystalline Fe at strain rates of 4.46×10^{-4}, 8.93×10^{-4}, 2.23×10^{-3}, 4.46×10^{-3}, 8.93×10^{-3} and $2.23 \times 10^{-2}\,s^{-1}$. Two nearly parallel lines can be drawn in each case as for Fig. 4, implying that twinning takes place as well as slip deformation at the higher strain rates. EBSD observations were not carried out on these specimens; however, some twins can be observed in SEM secondary imaging around cracks in specimens deformed at high strain rates (see Fig. 7). The slopes of the lines (i) and (ii) in Fig. 6(a), for polycrystalline Fe–3%Cr, give values of activation energy of 0.15 ± 0.07 eV and 0.14 eV, respectively. The slopes of lines (i) and (ii) in Fig. 6(b), from polycrystalline Fe, give values of activation energy of 0.21 ± 0.05 eV and 0.23 eV, respectively. Thus, as in Fe–9%Cr, it appears that dislocation glide is the controlling process over the whole strain rate range used, with the onset of twinning at high strain rates increasing T_c, possibly by inhibiting dislocation motion.

3.4. Activation energies for dislocation glide

Previous work on ductile–brittle transition in single-crystals has found that the activation energies deduced from DBT experiments are similar to those for dislocation glide [11–16]. Dislocation mobility data for the materials tested here are sparse. Data exist only for Fe, and then only for edge dislocations [25]; the DBT is most likely to be controlled by the motion of screw dislocations, which have much lower mobilities than edge dislocations in BCC metals [28].

The accepted model for screw dislocation motion in a BCC metal is by double-kink pair nucleation and propagation [29], giving a dependence of strain rate on temperature via a stress-dependent activation enthalpy for double-kink nucleation ($H_{kp}(\tau^*)$):

$$\dot{\varepsilon} = \dot{\varepsilon}_0 \cdot \exp(-H_{kp}(\tau^*)/kT), \tag{3}$$

where $\dot{\varepsilon}_0$ is a pre-exponential factor, T is the absolute temperature and (τ^*) is the local resolved shear stress on the dislocation. For values of applied shear stress (τ^*) much lower than the stress to move the dislocation without the operation of the double-kink mechanism (the 'Peierls stress', τ_p), $H_{kp}(\tau^*)$ is given by

$$H_{kp}(\tau^*) = 2H_k - 2\alpha(\tau^*)^{1/2}, \tag{4}$$

$$\text{where} \quad \alpha = \left(\frac{d^3 b \gamma_0'}{2}\right)^{1/2} \tag{5}$$

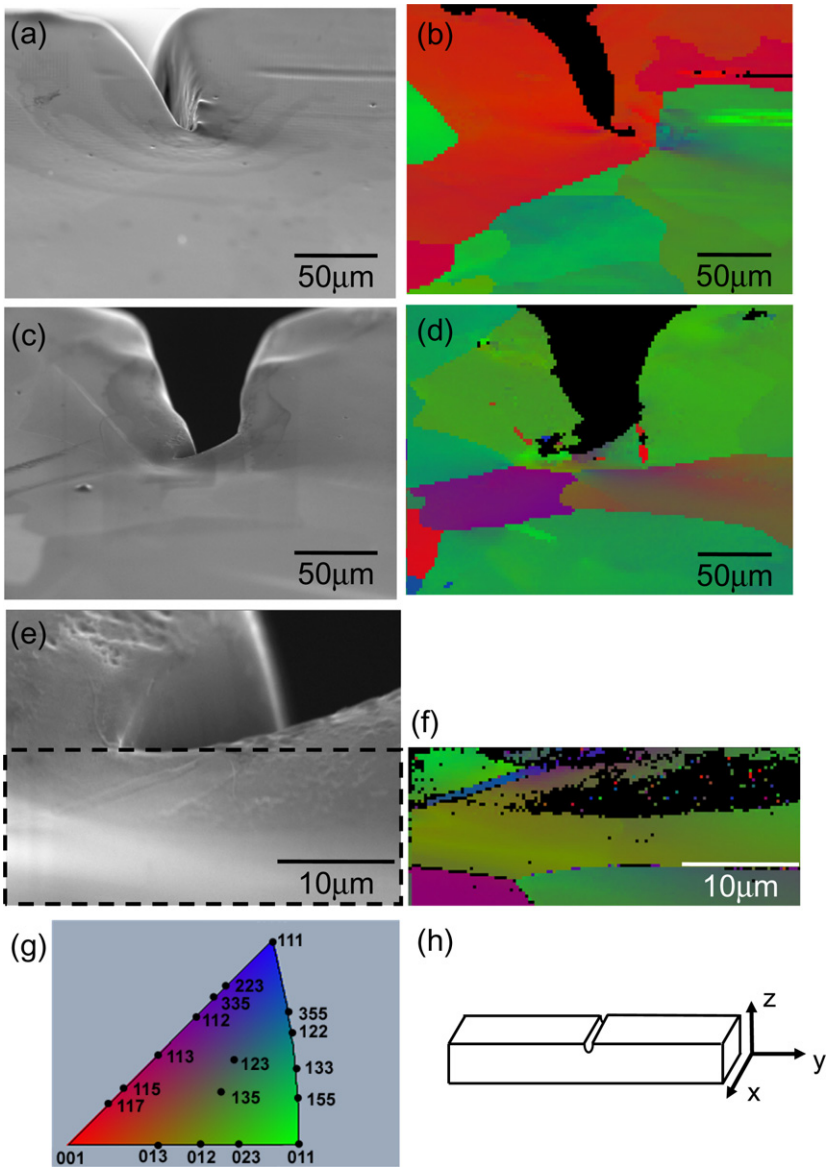

Fig. 5. (a) SEM image of a crack tip in a specimen of Fe–9%Cr deformed at $4.46 \times 10^{-4}\ s^{-1}$ (the lowest strain used); (b) EBSD image of the area in (a), indicating the crystallographic orientation of grains parallel to the x direction in (h); (c) SEM image of a crack tip in a specimen deformed at $8.93 \times 10^{-3}\ s^{-1}$ (the second-highest strain used for Fe–9%Cr); (d) EBSD image of the area in (a); twins are observed around the crack tip; (e) enlarged SEM image around the crack tip shown in (d); (f) EBSD image of the area surrounded by a dashed rectangle in (e). (g) Colour key used in (b), (c) and (f). (h) Schematic drawing of the sample and axis. All EBSD images show the crystallographic orientation parallel to the x direction of the sample.

and H_k is the single kink nucleation enthalpy in the absence of applied stress, d is the kink height, b is the magnitude of the Burgers vector, and γ_0 is the pre-logarithmic factor in the elastic part of the line tension of a dislocation [29]. For values of applied shear stress close to τ_p, Brunner [30] derived the following expression for the double-kink activation enthalpy:

$$H_{kp}(\tau^*) = 2H_k \frac{6}{5}\left[\frac{2}{3}\left(1-\frac{\tau^*}{\tau_p}\right)\right]^{5/4}. \quad (6)$$

Brunner and Diehl [30–32] obtained experimental values of $2H_k$ for pure iron by means of stress-relaxation tests, finding that $2H_k$ depended on the temperature range of the test: 0.93 eV for temperatures above 250 K (regime I), 0.74 eV for the temperature range between 120 K and 250 K (regime II), and 0.60 eV for temperatures below 120 K (regime III). The DBT temperatures found in this study for pure iron (100–120 K) are in regime II, where the experiments of Brunner and Diehl found $H_{kp}(\tau^*)$ to be 0.22–0.24 eV, with (τ^*) in their tests in the range 150–170 MPa, giving a good fit to Eq. (4), with $2H_k = 0.74$ eV and experimentally derived values for d, b and γ_0. A fit to Eq. (6) is possible with $\tau_p = 395$ MPa, which is plausible within this temperature range. Thus it is not clear which of Eq. (4) or (6) is best applicable to the experiments.

However, it is clear that experimental activation energies derived from strain rate variation of the ductile–brittle transition in iron are consistent with those obtained for dislocation motion in stress-relaxation tests, if the shear stresses on the dislocations active around the cracks are ~150 MPa. It is not very straightforward to obtain a value of such stresses in the ductile–brittle transition experiments, as the dislocations active around the crack tip will experience strong interaction stresses from nearby dislocations in addition to the strongly varying crack tip stress field and externally applied stresses. Tensile stresses at the specimen surface at fracture in these tests were typically 650 MPa, giving peak resolved shear stresses on the active dislocations of ~325 MPa; the values

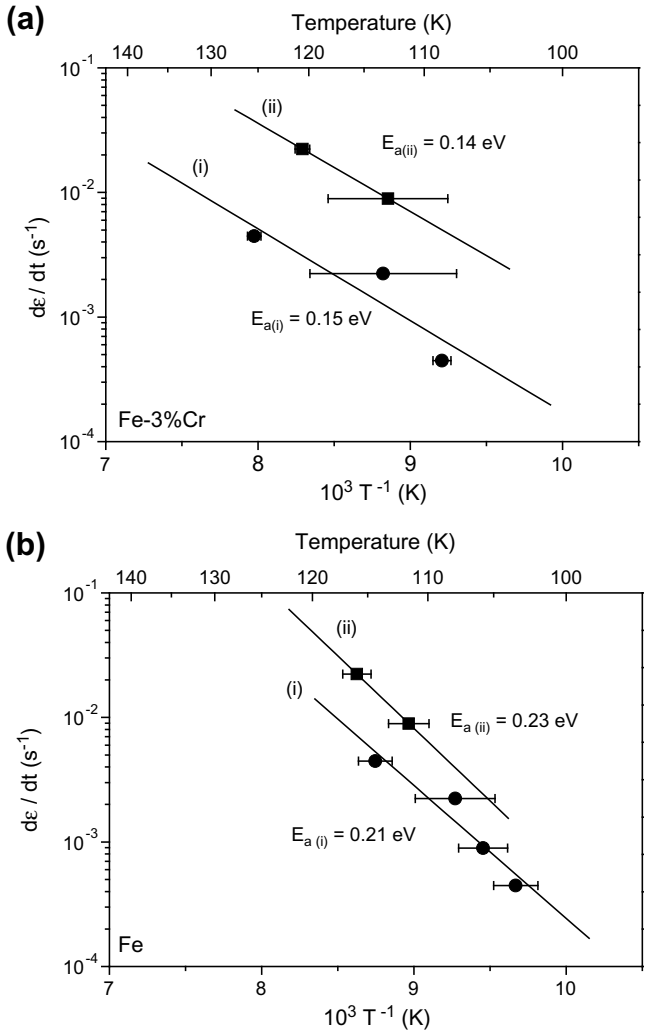

Fig. 6. Arrhenius plots of ln(strain rate) as a function of inverse transition temperaturefor: (a) polycrystalline Fe–3%Cr and (b) polycrystalline iron. Solid squares indicate strain rates where twinning was observed near the crack tip; solid circles indicate that no twinning was seen. For a given alloy composition, lines fitted to these two types of test results have the same slope, implying that the critical process in each case has the same activation energy. Error bars indicate the highest temperature for semi-brittle fracture and the lowest temperature for ductile bending.

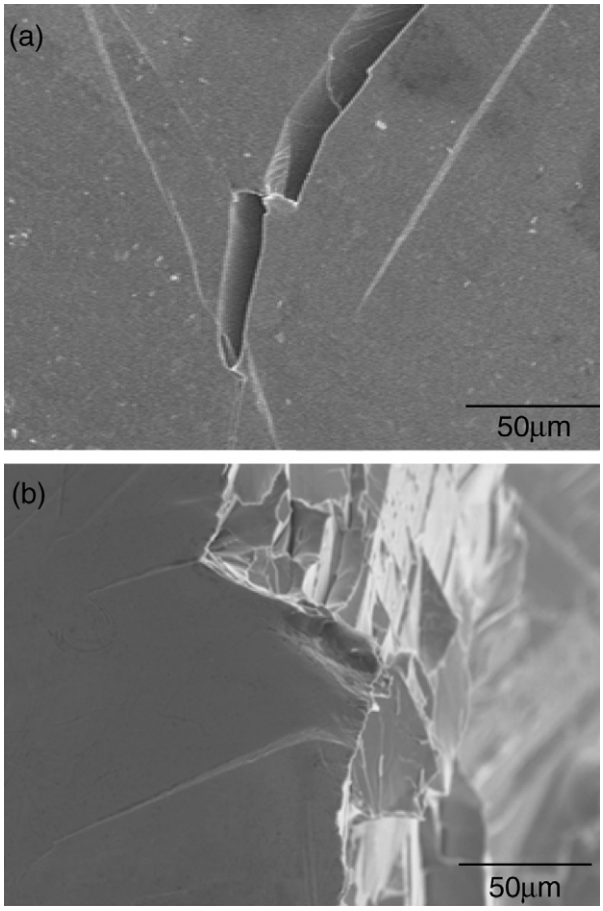

Fig. 7. SEM images around a crack, showing twins beside the crack. The strain rate used was $8.9 \times 10^{-3}\,s^{-1}$ (the second-highest strain rate), (a) polycrystalline Fe–3%Cr deformed at 111 K; (b) polycrystalline iron deformed at 116 K.

of stress below the tensile surface and in earlier parts of the loading cycle will range between zero and this peak value. The average values over the course of a fracture test are thus likely to be in the required range. Dislocation-dynamics models of the DBT in iron and iron–chromium alloys are currently being developed, and should give further insight into the crack tip deformation processes and local stresses on the dislocations.

4. Conclusions

The effect of chromium in iron on its ductile brittle transition (DBT) was experimentally studied, using chromium concentrations of 0%, 3% and 9% in polycrystalline iron. SEM and EBSD observations showed the development of some deformation twins as well as dislocation slip at crack tips deformed at high strain rates. The onset of twin deformation inhibits dislocation glide, which is the controlling process for the DBT at all strain rates. The value of activation energy for the DBT decreases with increasing chromium concentration in iron from 0.21 eV (Fe) though 0.15 eV (Fe–3%Cr) to 0.10 eV (Fe–9%Cr). This implies that the activation energy for dislocation glide in iron–chromium alloys varies similarly with chromium content. The activation energy found for iron is consistent with that for screw dislocation motion by the double-kink mechanism. Hence it is likely that the presence of chromium modifies the activation parameters of this process. The lowering of the activation energy for screw dislocation glide is also likely to be related to the phenomenon of low-temperature solution softening observed in many BCC binary systems [33]; in particular, iron–chromium binary alloys exhibit a hardness decrease with increasing chromium content up to ~8% below 190 K.

Acknowledgements

The authors gratefully acknowledge the financial support of UKAEA Culham Laboratories, and helpful discussions with Professor S.L. Dudarev.

References

[1] A. Kohyama, A. Hishinuma, D.S. Gelles, R.L. Klueh, W. Deitz, K. Ehrlich, J. Nucl. Mater. 233–237 (1996) 138.
[2] K. Ehrlich, Fus. Eng. Des. 56&57 (2001) 71.
[3] R. L Klueh, J.M. Vitek, W.R. Corwin, D.J. Alexander, J. Nucl. Mater. 155–157 (1988) 973.
[4] A. Hishinuma, A. Kohyama, R.L. Klueh, D.S. Gelles, W. Deitz, K. Erlich, J. Nucl. Mater. 258–263 (1998) 193.
[5] R.L. Klueh, M.A. Sokolov, K. Shiba, Y. Miwa, J.P. Robertson, J. Nucl. Mater. 283 (2000) 478.
[6] D.S. Gelles, J. Nucl. Mater. 225 (1995) 163.

[7] A. Kohyama, A. Hishinuma, D.S. Gelles, R.L. Klueh, W. Deitz, K. Erlich, J. Nucl. Mater. 233–237 (1996) 138.
[8] D. Hull, P. Beardmore, A.P. Valintine, Philos. Mag. 14 (1965) 1021.
[9] P. Gumbsch, J. Riedle, A. Hartmaier, H.F. Fischmeister, Science 282 (1998) 1293.
[10] T.D. Joseph, M. Tanaka, A.J. Wilkinson, S.G. Roberts, J. Nucl. Mater. 367–370 (2007) 637.
[11] A. Giannattasio, S.G. Roberts, Philos. Mag. 87 (2007) 2589.
[12] K.F. Ha, C. Yang, J.S. Bao, Scr. Metall. Mater. 30 (1994) 1065.
[13] C. St. John, Philos. Mag. 32 (1975) 1193.
[14] J. Samuels, S.G. Roberts, Proc. R. Soc. Lond. A 421 (1989) 25.
[15] H.S. Kim, S.G. Roberts, J. Am. Ceram. Soc. 77 (1994) 3099.
[16] A. Giannattasio, M. Tanaka, T.D. Joseph, S.G. Roberts, Phys. Scr. T 128 (2007) 87.
[17] F.C. Serbena, S.G. Roberts, Acta Metall. Mater. 42 (1994) 2505.
[18] S. Fujita, K. Maeda, S. Hyodo, Philos. Mag. A 65 (1992) 131.
[19] P. Pirouz, M. Zhang, J.L. Demenet, H.M. Hobgood, J. Appl. Phys. 93 (2003) 3279.
[20] A.S. Booth, S.G. Roberts, Acta Mater. 45 (1997) 1017.
[21] F.C. Serbena, DPhil thesis, University of Oxford, 1995.
[22] P.B. Hirsch, A.S. Booth, M. Ellis, S.G. Roberts, Scr. Metall. Mater. 27 (1992) 1723.
[23] P.B. Hirsch, S.G. Roberts, Philos. Mag. 64 (1991) 55.
[24] S.G. Roberts, in: J. Lepinoux et al. (Eds.), Proceedings of the Conference Multiscale Phenomena in Plasticity, Kluwer Academic Press, Netherlands, 2000, p. 349.
[25] A.P.L. Turner, T. Vreeland, Scr. Metall. 4 (1970) 913.
[26] T.L. Altshuler, J.W. Christian, Philos. Trans. R. Soc. Lond. 261 (1967) 253.
[27] W.F. Brown Jr., J.E. Srawley, ASTM STP 410 (1966) 1.
[28] V. Vitek, M. Yamaguchi, J. Phys. F3 (1973) 537.
[29] J.P. Hirth, J. Lothe, Theory of Dislocations, McGraw-Hill, Inc., 1968. p. 496.
[30] D. Brunner, J. Diehl, Phys. Status Solidi (a) 124 (1991) 455.
[31] D. Brunner, J. Diehl, Phys. Status Solidi (a) 124 (1991) 155.
[32] D. Brunner, J. Diehl, Phys. Status Solidi (a) 125 (1991) 203.
[33] J.R. Stephens, W.R. Witzke, J. Less-Common Met. 48 (1976) 285.